PHYSICAL REVIEW A **84**, 032517 (2011)

Calculation of supercritical Dirac resonance parameters for heavy-ion systems from a coupled-differential-equation approach

A. Marsman[*] and M. Horbatsch[†]
Department of Physics and Astronomy, York University, Toronto, Ontario M3J 1P3, Canada

(Received 20 July 2011; published 27 September 2011)

Previous work [E. Ackad and M. Horbatsch, Phys. Rev. A **78**, 062711 (2008)] on supercritical Dirac resonance parameters from extrapolated analytic continuation, obtained with a Fourier grid method, is generalized by numerically solving the coupled Dirac radial equations to a high precision. The equations, which contain the multipole decomposition of the two-center potential, are augmented by a complex absorbing potential and truncated at various orders in the partial wave expansion to demonstrate convergence of the resonance parameters in the limit of vanishing absorber. The convergence of the partial-wave spinor and of the multipole potential expansions is demonstrated in the supercritical regime. The comparison of critical distances with literature values shows that the work provides benchmark results for future two-center calculations without multipole expansion.

DOI: 10.1103/PhysRevA.84.032517 PACS number(s): 31.30.J−, 31.15.−p, 14.60.Cd, 12.20.−m

I. INTRODUCTION

The Dirac spectrum of a relativistic electron in the modified Coulomb potential of a finite-size atomic nucleus is characterized by positive- and negative-energy continuum states, with discrete bound states occurring in the gap between m_ec^2 and $-m_ec^2$. As the nuclear charge Z increases, the bound-state energies decrease sharply, until a critical value of $Z_{\rm cr} \approx 170$ is reached, beyond which the ground state "dives" into the negative continuum, i.e., $E_{1s} < -m_ec^2$ [1–3].

This supercritical potential now supports resonance states, whereby a vacant $1S\sigma$ state can couple to the filled negative-energy continuum. According to the Dirac sea interpretation, a negative-continuum electron can then tunnel into the region near the nucleus and become bound, while the resulting hole can be interpreted as an emitted positron. Alternately, the empty electronic "hole" can be seen as a quasibound positron that escapes to infinity as the resonance decays. This leads to the breakdown of the unstable QED vacuum and decay by pair creation into a charged state, resulting in a bound electron and emission of a free positron [1,2].

While the Dirac sea interpretation is superseded by quantum field theory, expressions derived within QED for exclusive and inclusive pair production processes [4] are fully consistent with the present Dirac equation treatment. The present treatment allows one to employ the powerful apparatus of quantum mechanical resonance methods based on analytic continuation and extrapolation.

In analogy to more familiar resonances in the positive continuum (e.g., Stark resonances), supercritical Dirac resonances are described by their mean energy position $E_{\rm res}$ and lifetime τ . In a scattering system, this corresponds to a peak in the total cross section, which can be described by a Breit-Wigner shape having a peak at the resonance energy and a width Γ that is related to the lifetime of the state by the uncertainty principle: $\Gamma\tau \sim \hbar$. Since supercritical resonances have negative energy, they correspond to positrons emitted with kinetic energy given by $|E_{\rm res} + 511 \text{ keV}|$.

While there are no naturally existing superheavy nuclei with charge $Z \geqslant 170$, supercritical phenomena can be investigated experimentally through heavy-ion collisions near the Coulomb barrier, wherein the nuclei approach within a critical distance and their combined fields are strong enough to support resonance states and subsequent decay of the neutral vacuum.

Calculations [5–7] for collision systems like U-U predict widths in the kilo–electron volt range, which correspond to lifetimes of the order of 10^{-19} s. While this is relatively long-lived compared to the collision time, there is a finite probabilty that the resonance will decay while the nuclei are within a supercritical distance. It is also possible that "sticky" (inelastic) collisions extend the collision time before the decay of a compound nucleus [8].

The process of spontaneous positron emission, accompanied by electron filling of the $1S\sigma$ vacancy, is distinct from dynamical pair creation processes during the collisions. Other positron production processes compete with the spontaneous decay of the vacuum, e.g., the electromagnetic field of the moving nuclear charges (negligible near the critical distance, as the nuclei slow down) and pair-conversion of hard photons emitted by decay of excited nuclear states.

An adiabatic treatment of the electronic motion is justified, as the motion of the target ions is sufficiently slow for the electrons to rapidly adjust to the changing nuclear potential, especially near closest approach. The nuclear motion is therefore treated using classical scattering trajectories, where at any instant of time, the electrons feel the combined potential due to the nuclei at their current positions $R_{1,2}(t)$. Such an approach can take advantage of solution of two-center Dirac stationary states, which are used as a basis when computing the full, time-dependent nuclear collision.

The stationary eigenvalue problem has been solved using a matrix representation of the Hermitian two-center Hamiltonian [5,9]. The electronic states are expanded in terms of a sine basis sampled on a discrete spatial mesh, and diagonalization of the supercritical Dirac Hamiltonian yields a set of discretized quasicontinuum states. The supercritical resonance is thus represented as a superposition of these continuum states. The mean energy and width of the resonance can then be obtained by fitting a Breit-Wigner shape to the density of states or

---

[*] amarsman@yorku.ca

[†] marko@yorku.ca

to the overlap of the continuum states with a reference $1S\sigma$ subcritical bound state [5].

A more accurate determination of the resonance parameters can be obtained through the use of analytic continuation methods, which transform the original Hamiltonian into a non-Hermitian operator with complex eigenenergies and whose eigenfunctions are bounded, square-integrable solutions. The supercritical resonance is now represented by a single state in the spectrum, allowing for a more accurate determination of the position and width parameters from the eigenenergy: $E_R = E_{\text{res}} + i\Gamma/2$. The sign of the width is positive for resonances in the negative-energy continuum, as we interpret the supercritical electron resonance as corresponding to a positive-energy antiparticle traveling backward in time. *CPT* symmetry thus requires a positive imaginary part to represent a decaying state as time propagates to negative infinity.

One particular method of analytic continuation is the addition of a scalar complex absorbing potential (CAP) to the Dirac Hamiltonian,

$$\hat{H}_{\text{CAP}} = \hat{H} - i\eta\hat{\beta}\Theta(r - r_c)(r - r_c)^2, \tag{1}$$

where $\hat{\beta}$ is the standard Dirac matrix and $\eta \geqslant 0$ is a small parameter that sets the strength of the CAP. The range parameter r_c, which appears in the Heaviside function, as well as in the quadratic factor, determines the point at which the CAP turns on. Its value is chosen so that the CAP is only active outside the bound-state portion of the resonance wave function and, thus, dampens the continuum part of the wavefunction at large radial distances.

The solution of the Dirac equation with a CAP-augmented Hamiltonian, for a particular choice of r_c and using a range of η values, results in an eigenenergy trajectory $E_R(\eta)$ in the complex plane. As the value of the strength parameter is decreased, the energy eigenvalues smoothly approach the true position of the resonance, stabilizing at some small value of η, until the path deviates unpredictably below a critical value η_{crit}.

For $\eta < \eta_{\text{crit}}$ the solution based on a finite matrix representation fails, since it cannot resolve the oscillating tail of the resonance wave function (the CAP is too weak). However, for finite η the added CAP makes the Hamiltonian somewhat unphysical. In the stabilization method one seeks minimal dependence of the eigenvalue on η. In the extrapolated or continuation method one seeks the $\eta \to 0$ limit on the basis of finite-η calculations. One constructs a rational function approximation to a segment of the $E_R(\eta)$ trajectory where $\eta > \eta_{\text{crit}}$ [10]. This complex-valued Pade approximant is then extrapolated to a zero argument to arrive at the best estimate of the resonance parameters: $E_R^* = E_{\text{Pade}}\ (\eta = 0)$.

While the solution by matrix methods yields robust and consistent values for the resonance parameters, it depends on a sufficiently large N of the basis set and encounters difficulties in accurately representing the nonperiodic (exponentially decaying) resonance wave functions at large radial distances. For calculations beyond the monopole approximation to the two-center potential, the size of the Hamiltonian matrix also depends on the number of coupled angular momentum channels N_κ, resulting in a $(2 \cdot N \cdot N_\kappa) \times (2 \cdot N \cdot N_\kappa)$ matrix.

In the present work we develop a CAP-based solution based on direct numerical integration of the radial Dirac equations to find the complex energy eigenvalues. The aim of this work is to explore the η dependence on the basis of differential equation solvers which adjust grid points adaptively in order to satisfy a preset tolerance criterion. The method allows us to use small η values, since it does not suffer from the finite-η discrete-variable representation problems in the asymptotic regime. This method is shown to be practical, since there are fewer limitations imposed on the number of partial waves that can be coupled.

II. METHODS

The nuclear system (Z_1,A_1)-(Z_2,A_2) is modeled as a pair of uniformly charged spheres of radius $R_n^{(1)}$ and $R_n^{(2)}$, where $R_n^{(1,2)} = 1.2(A^{(1,2)})^{1/3}$ fm. The nuclei are separated by a distance R and displaced along the z axis from their center of mass by $r_{\text{cm}}^{(1)}$ and $r_{\text{cm}}^{(2)}$, respectively. The stationary Dirac equation with this minimally coupled two-center Coulomb potential is given in natural units ($\hbar = c = m_e = 1$) as

$$[\hat{\alpha} \cdot \hat{p} + \hat{\beta} + V_{TC}(\vec{r})]\Psi(\overrightarrow{r}) = E\Psi(\overrightarrow{r}). \tag{2}$$

The two-center system is not separable into radial and angular parts, but a good quantum number characterizing the eigenfunctions is μ, the angular-momentum projection on the z axis. If both nuclei are identical, the charge symmetry also allows the wave functions to have good parity (even or odd). The presence of azimuthal symmetry motivates an expansion of the potential in terms of Legendre polynomials:

$$V_{TC}(\vec{r},R) = \sum_{l=0}^{\infty} V_l(r,R)P_l(\cos\theta). \tag{3}$$

The wave function is expanded in a spherical-spinor basis

$$\Psi_\mu(\overrightarrow{r}) = \frac{1}{r}\sum_{\kappa=\pm1}^{\pm\infty}\begin{pmatrix} g_\kappa(r)\chi_\kappa^\mu \\ if_\kappa(r)\chi_{-\kappa}^\mu \end{pmatrix}, \tag{4}$$

where $\kappa = \pm(j + \frac{1}{2})$ labels the total angular momentum, and the spherical spinors χ_κ^μ carry angular and spin dependence.

Substituting (3) and (4) into the Dirac equation and projecting onto $\langle\chi_\kappa^\mu|$, $(\kappa = \pm1, \pm2, \ldots, \pm\infty)$ yields the radial equations [3]:

$$\begin{aligned}\frac{dg_\kappa}{dr} &= -\frac{\kappa}{r}g_\kappa + (1+E)f_\kappa \\ &\quad - \sum_{\bar{\kappa}=\pm1}^{\pm\infty}\left\{\sum_{l=0}^{\infty}V_l(r,R)\langle\chi_{-\kappa}^\mu|P_l|\chi_{-\bar{\kappa}}^\mu\rangle\right\}f_{\bar{\kappa}},\end{aligned} \tag{5}$$

$$\frac{df_\kappa}{dr} = \frac{\kappa}{r}f_\kappa + (1-E)g_\kappa + \sum_{\bar{\kappa}=\pm1}^{\pm\infty}\left\{\sum_{l=0}^{\infty}V_l(r,R)\langle\chi_\kappa^\mu|P_l|\chi_{\bar{\kappa}}^\mu\rangle\right\}g_{\bar{\kappa}}. \tag{6}$$

This infinite set of coupled differential equations is then truncated by selection of a suitable cutoff in both the number of channels in the basis and in the multipole order of the two-center potential.

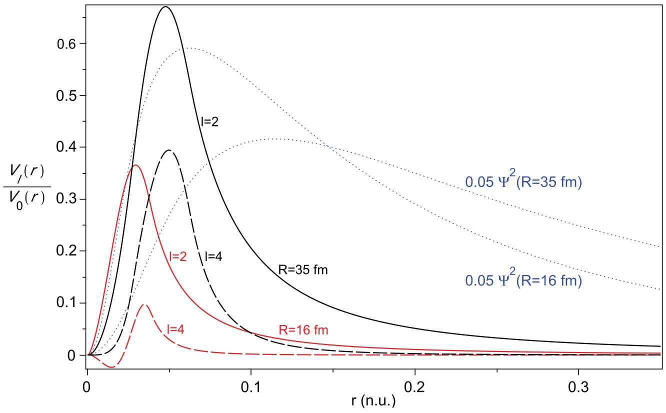

FIG. 1. (Color online) Ratio of higher-order multipole strengths to the dominant monopole potential in the U-U system, as a function of radial distance in natural units, for two internuclear separations. Black, $R = 35$ fm; red, $R = 16$ fm. Solid line, $l = 2$; long-dashed line, $l = 4$. The corresponding radial density for each case (a bound state for $R = 35$, a resonance for $R = 16$) is shown by the dotted (blue) line.

A. Channel coupling and the multipole expansion

The matrix elements $\langle \chi_{\kappa,\mu}|P_l|\chi_{\bar{\kappa},\mu}\rangle$ that couple the various angular-momentum channels are calculated using Clebsch-Gordan coefficients and Gaunt's formula [11]. With increasing multipole order, channels are coupled whose orbital angular momentum sectors are similarly separated, e.g., the monopole only couples channels diagonally, the dipole potential involves channels where $\Delta l = \pm 1$, the quadrupole when $\Delta l = 0, \pm 2$, the octopole for $\Delta l = \pm 1, \pm 3$, and the hexadecapole when $\Delta l = 0, \pm 2, \pm 4$. The dominant $1S_{1/2}$ channel thus couples both directly (and with similar strength) to all other channels and, also, indirectly via transitive couplings, which fall off more quickly.

The channel couplings are mediated by the multipole potentials $V_l(r,R)$, and the $l = 0$ monopole contribution, with its long-range tail and high strength, dominates at all distances. However, the effects of the higher-order multipoles, especially in the supercritical regime, should not be discounted, as Fig. 1 illustrates. Here, the ratios of the $l = 2$ and $l = 4$ multipoles to the monopole potential in the U-U system are shown for two nuclear separations: $R = 16$ fm, which is close to the Coulomb barrier, and $R = 35$ fm, which is close to the critical distance. The odd-order contributions are identically 0 due to the charge symmetry of the system. The $l = 2$ and $l = 4$ multipoles are quite pronounced. While these components are strong at short range only, the resonance wave function is highly localized and samples these multipole contributions efficiently, as is evident in the figure. Inclusion of these higher orders in the truncated equations results in appreciable shifts in the resonance position and, more significantly, in a marked broadening of the resonance widths, especially at larger values of R.

B. Bound-state energies

As the first step, we seek the bound-state energies in a subcritical nuclear potential. The coupled equations for a selected set of angular-momentum channels and multipole terms are integrated twice: outward from a small radius near the origin and inward from a large "asymptotic" radius r_a. The solutions are computed to an intermediate matching radius, and the error is minimized using a Newton-Raphson iteration process to determine the values of the energy and coefficients for the initial conditions that correspond to a bound state.

For each channel, the initial conditions at the origin (to an arbitrary multiplicative constant) are derived from a power-series ansatz [12]:

$$\begin{pmatrix} g_\kappa \\ f_\kappa \end{pmatrix} \sim r^{|\kappa|} \sum_{n=0}^{\infty} \begin{pmatrix} a_{\kappa n} \\ b_{\kappa n} \end{pmatrix} r^n. \tag{7}$$

Substitution of this form into the coupled radial equations leads to recurrence relations for the coefficients $\{a_{\kappa n}, b_{\kappa n}\}$. Only the leading-order terms are included.

The wave functions at the outer radius are obtained by making the approximation that the higher order multipoles vanish rapidly at large distances, and only the monopole nuclear potential is important. This decouples each channel, and with the further assumption that the potential remains constant for $r \geqslant r_a$, the individual radial equations are solved analytically in this region. This solution provides boundary value conditions at $r = r_a$ to start the inward integration. The numerical integration was performed with a variety of adaptive-step algorithms, including Runge-Kutta-Fehlberg-4/5 and a Gear/BDF implementation, and all of them gave values for the eigenenergies that differed by 10^{-12} to 10^{-14}.

The $1S\sigma$ bound-state energies are thus calculated for a range of subcritical internuclear separations R, for which the eigenenergy approaches the negative continuum from above. A polynomial fit $E(R)$ is found, and extrapolation then yields the critical distance D_c as the solution to $E(D_c) = -1$.

C. Supercritical resonances

The supercritical regime is now explored with the addition of the CAP. Since it enters into the Dirac equation as a scalar quantity, in the radial equations it appears in the second term on the right-hand sides:

$$\frac{dg_\kappa}{dr} = -\frac{\kappa}{r} g_\kappa + (1 + E + V_{\text{CAP}}) f_\kappa + \cdots, \tag{8}$$

$$\frac{df_\kappa}{dr} = \frac{\kappa}{r} f_\kappa + (1 - E + V_{\text{CAP}}) g_\kappa + \cdots. \tag{9}$$

An integration and matching procedure is followed as before, except that the eigenenergy and initial condition coefficients are now complex numbers. For any given supercritical internuclear separation, the effect of varying the CAP parameters is then determined. For given choices of CAP radius parameter r_c, complex-energy trajectories are generated by gradually reducing the CAP strength η.

The CAP trajectories are of two basic types, depending on the size of the internuclear separation. The first type, which is observed for small values of R, exhibits a smooth and stable curve down to a critical value of η, below which the path deviates unpredictably. The trajectory for larger r_c tends to becomes unstable at a larger value of η, as a stronger CAP is needed to attenuate the oscillatory tail of the wave function over the shrinking region from the CAP effective radius r_c to the asymptotic radius r_a. The position of the stabilization point η_{stab} is obtained in practice from $\min\{|\eta \frac{dE(\eta)}{d\eta}|\}$ and then examined to see how it behaves as a function of r_c.

Selecting those CAP trajectories that stabilize closest to a common average point, a Padé approximant is used to extrapolate them to $\eta = 0$. Figure 2 shows the extrapolated values for some candidate CAP trajectories and the variance of the resonance parameters as a function of the starting point i_0 of a fourth-order Padé fit, expressed as the distance from the stabilization point, i.e., $i_0 \Delta\eta$. After selecting the starting point which minimizes the variation of the extrapolated values among trajectories, an average resonance eigenvalue is obtained, minimizing dependence on the choice of CAP radius. Higher order fits ($N_p = 6$, $N_p = 8$) were also tried and give comparable accuracies.

Figure 2(c) shows the same CAP trajectories generated using a larger outer radius ($r_a = 35$). Evidently, increasing r_a results in a more accurate representation of the asymptotic wave function, and thus the larger region over which the CAP is active yields trajectories that are stable at smaller values of η. This allows for a more accurate extrapolation to the true resonance parameters.

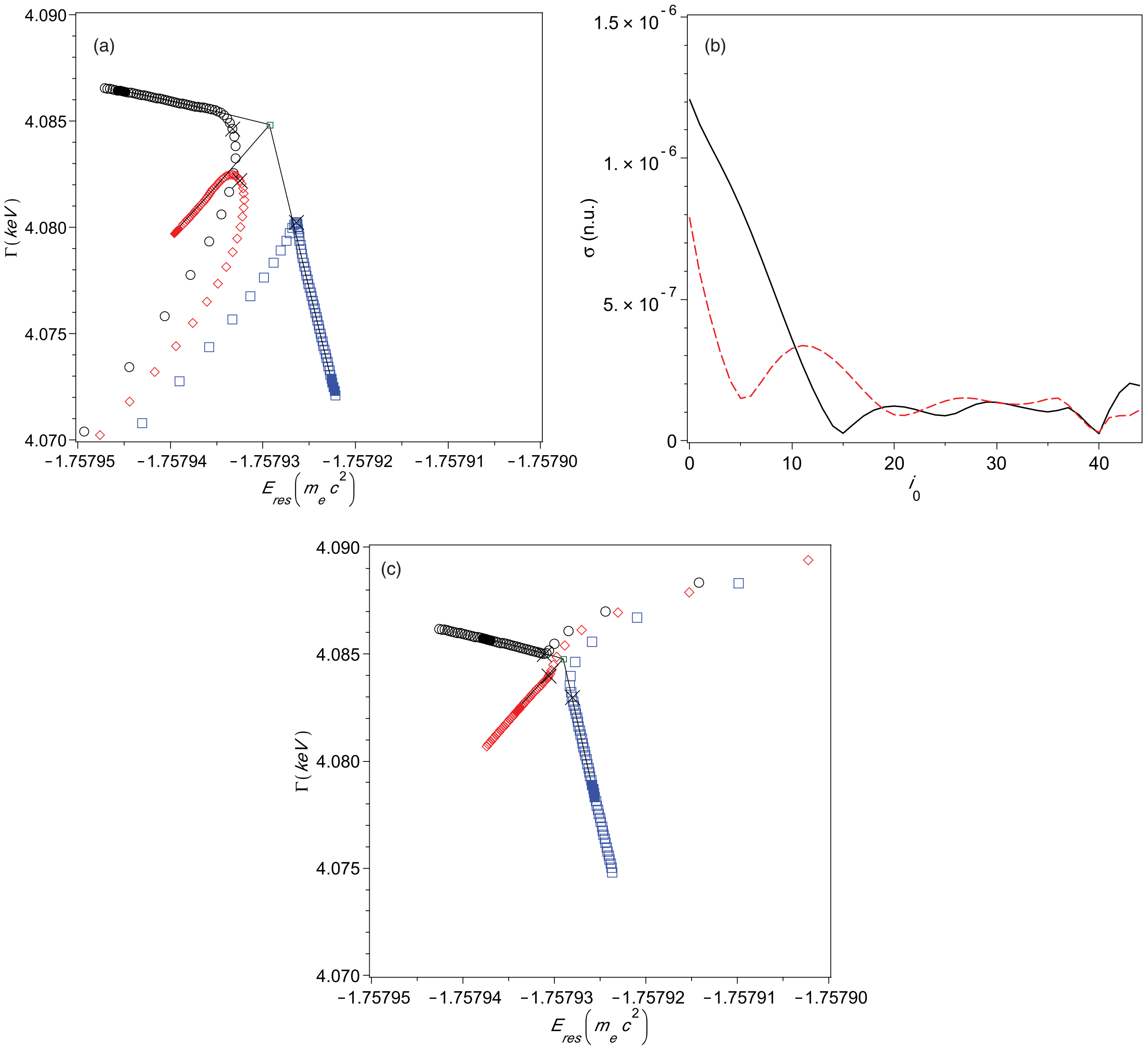

FIG. 2. (Color online) Extrapolated CAP trajectories for the U-Cf system at a separation of $R = 20$ fm. The CAP strength is reduced from $\eta = 0.007$ to $\eta = 0.0001$ (in steps of $\Delta\eta = 0.0001$). (a) Trajectories for $r_c = 4.0$ 5.0, and 7.0 extrapolated using an $N_p = 4$, $i_0 = 40$ Padé fit. Stabilization points are shown as (black) crosses. The $N_p = 4$ points used for the fit are shown by the filled symbols, and the average extrapolated value is shown as the green box. Eigenenergies were obtained with $r_a = 25$. (b) Absolute variance of extrapolated energy [solid (black) line] and width [dashed (red) line] in natural units, as the initial point i_0 for the Padé fit is varied. Here i_0 measures the distance from the stabilization point, $i_0 \Delta\eta$. (c) The same CAP trajectories as in (a) computed using a larger outer radius, $r_a = 35$.

TABLE I. Accuracy of resonance parameters with increasing outer integration radius r_a (in natural units) for the U-Cf system at $R = 20$ fm.

r_a	E ($m_e c^2$)	Γ (keV)
20	−1.75793	4.08
25	−1.757929	4.0848
30	−1.7579290	4.08478
35	−1.75792904	4.08478
40	−1.75792904	4.08478

Table I shows the resonance position and width of the U-Cf system at a separation of $R = 20$ fm, calculated with increasing values of r_a. Calculations with larger r_a are more computationally intensive, and using values of r_a greater than about 40 is numerically unstable. We find that the accuracy of the computed values converges to the digits shown when $r_a = 35$, hence this nominal value was used for all further calculations. . .

For larger internuclear separations (around $R = 35$ fm and above in the U-Cf system, $R = 25$ fm for U-U), the CAP trajectories have a different character. They remain stable and approach the resonance eigenvalue smoothly as η is decreased. These curves can be extrapolated to a very high accuracy, as they can be generated using very small η values (of the order 10^{-7} to 10^{-8}, below which convergence of the eigenvalue solution becomes a limiting factor), approaching the true resonance point very closely. As R approaches the critical distance, the resonance width decreases rapidly, and the amplitude of the wave function's oscillatory tail diminishes in comparison to the bound part, requiring a much weaker absorber to render the state square-integrable.

A comparison of Figs. 2(a) and 2(c) demonstrates the strength of the present coupled-differential equations approach. Limiting the wave functions in the asymptotic regime to the constant-potential solution (i.e., choosing a smaller r_a value) yields trajectories similar to those obtained in the mapped-Fourier grid method [6]. Extending the numerical integration of the equations well into the asymptotic regime allows us to rely much less on extrapolation to remove artifacts of the CAP.

III. RESULTS

A. Critical distances

We now examine the critical distance for various heavy-ion systems. This is the internuclear separation at which the energy of the ground state dives into the negative-energy continuum. The even-parity ground-state energy $E_{1S\sigma_g}$ was computed for a range of separations close to the critical distance, and a polynomial fit was used to extrapolate the distance down to the boundary of the negative continuum ($E = -mc^2$). Table II lists the computed values for various homonuclear one-electron quasimolecules $A_2^{(2Z-1)+}$, as increasing angular-momentum channel couplings (κ) are taken into account, with the inclusion of higher multipole orders (l) in the two-center potential.

The nuclear symmetry causes all the odd-order multipoles to vanish identically, thus coupling channels with even angular-momentum quantum number l separately from those with odd l. These two distinct sets of coupled equations correspond to the even- and odd-parity eigenstates, respectively.

Table II lists some critical distances (D_c) obtained by other authors [13–15]. Comparing our values of D_c (using the $l = 4$ multipole and up to the $\kappa = 4$ channel) with these other results, we see a general agreement in magnitude, but also some deviations. There are a number of reasons for these discrepancies.

One difference is due to the basic method for the solution of the two-center Dirac problem. While we integrate the radial equations numerically, Refs. [13] and [15] use various basis-set expansions to approximate the bound states of the system, while in Ref. [14] the problem is solved variationally. Expansion of the wave function and potential also means that an increasingly larger set of channels/multipoles is required to converge to the true value. In contrast, the use of elliptical/prolate-spheroidal coordinates in [13,16] eliminates the multipole truncation effects inherent in our approach, as the two-center potential is represented in its entirety.

Another important factor is the model of the nuclear charge. Our work represented the nuclei as uniformly charged spheres of specified radius R_n, while other calculations [15] account for the finite nuclear size using the Fermi model of the nuclear charge distribution, characterized by a root-mean-square charge radius $\langle R_n^2\rangle^{1/2}$ and a gradual falloff with radial distance.

TABLE II. Critical distances D_c (fm) for homonuclear one-electron quasimolecules $A_2^{(2Z-1)+}$. *Values calculated using $\kappa = -1, +2, -3$. †Values obtained with $\kappa = -1, +2, -3, +4$. Column 9 provides effective radii according to Ref. [15], while column 10 lists our corresponding most-converged results for the critical distances.

Z	R_n(fm)	$l_{\max} = 0$	$l_{\max} = 2$		$l_{\max} = 4$		Other work	$\tilde{R}_n$(fm)	$\widetilde{D}_c$(fm)
88	7.309	19.0799	19.7616*	19.7622†	19.7593*	19.7583†	19.91,[a]19.4[b]	7.191	19.8758†
90	7.374	25.6651	26.9015*	26.9032†	26.8937*	26.8903†	27.05,[a]26.5[b]	7.386	26.8808†
92	7.437	32.6217	34.4812*	34.4847†	34.4668*	34.4605†	34.72,[a]34.3,[b]34.7[c]	7.561	34.3805†
94	7.499	40.0043	42.5417*	42.5475†	42.5210*	42.5125†	43.16,[a]42.6[b]	7.480	42.5224†
96	7.529	47.8263	51.0977*	51.1063†	51.0716*	51.0627†	52.09,[a]51.6[b]	7.508	51.0722†
98	7.570	56.0564	60.1118*	60.1238†	60.0818*	60.0748†	61.63,[a]61.0,[b]61.1[c]	7.545	60.0846†

[a] From Ref. [15]

[b] From Ref. [14].

[c] From Ref. [13]

TABLE III. Critical distance D_c (fm) of the (U-Cf)$^{189+}$ system. *Configurations that do not introduce new coupling terms in the equations. †Values computed using the effective radii $\tilde{R}_n$ for the nuclear species.

	Multipole cutoff					
Channel	$l_{\max} = 0$	$l_{\max} = 1$	$l_{\max} = 2$	$l_{\max} = 3$	$l_{\max} = 4$	
$\kappa = -1$	43.894	—	—	—	—	—
$\kappa = \pm1$	—	43.894	43.894*	43.894*	43.894*	43.878†
$\kappa = \pm1, -2$	—	43.909	43.910	43.910*	43.910*	43.895†
$\kappa = \pm1, \pm2$	—	43.909	43.483	43.483	43.483*	43.468†
$\kappa = \pm1, \pm2, -3$	—	43.909	46.815	46.814	46.791	46.770†
$\kappa = \pm1, \pm2, \pm3$	—	43.909	46.815	46.815	46.792	46.771†
$\kappa = \pm1, \pm2, \pm3, -4$	—	43.909	46.816	46.819	46.796	46.775†
$\kappa = \pm1, \pm2, \pm3, \pm4$	—	43.909	46.823	46.826	46.787	46.767

To investigate the effect of the nuclear model, the critical distance calculations were repeated using a prescription in [17], where an arbitrary nuclear model can be closely approximated by a uniformly charged sphere with an appropriately chosen radius. To first order, this effective radius is given by $\tilde{R}_n = \sqrt{\frac{5}{3}}\langle R_n^2\rangle^{1/2}$, where $\langle R_n^2\rangle^{1/2}$ is the root-mean-square radius of the charge distribution. Using the same rms values listed in [15], the last two columns in Table II list the corresponding effective radius and revised critical distance for each nuclear system. The calculations used the maximum number of channels and multipole orders available. The critical distance D_c in most cases changes by only 0.01 fm. One exception is $Z = 88$, where the original radius corresponds to Ra^{226}, while the new effective one is for the Ra^{214} isotope. We note that the U^{238} nucleus is assigned an unusually large rms radius in [15], following [18].

For the asymmetric (U-Cf)$^{189+}$ system, parity is no longer a good quantum number. All angular momentum channels are coupled via higher-order multipole components and, thus, contribute to the $1S\sigma$ ground state. Table III shows the critical distance D_c as more channels are included, and the multipole expansion is truncated at increasing order.

The table shows that for a fixed multipole cutoff $l_{\max}$ the κ expansion converges rapidly. The change in D_c is not monotonic. An increase in $l_{\max}$ from 3 to 4 leads, however, to a roughly 5% increase when the $\kappa = \pm4$ channels are included. The calculation truncated at $l_{\max} = 4$ and $|\kappa_{\max}| = 4$ results in $D_c \approx 46.79$ fm, which is to be compared to $D_c = 47.7$ fm in [13], derived using a more converged basis expansion calculation. Since our emphasis is on resonance parameter calculations, i.e., the supercritical regime, we did not pursue calculations with $l_{\max} > 4$. Table II clearly shows that the multipole truncation becomes problematic for the highest case, $Z = 98$. The critical distances of $D_c \approx 60$ fm from our work fall short of the $D_c \gtrsim 61$ fm two-center results.

The last column in Table III lists the critical distances calculated using the effective radii $\tilde{R}_n^U = 7.561$ fm and $\tilde{R}_n^{\mathrm{Cf}} = 7.545$ fm, where we see that the original results are reduced by about 0.02 fm.

B. Supercritical resonance parameters

For nuclear separations smaller than the critical distance, the $1S\sigma$ ground state enters the negative energy continuum and becomes a resonance due to the coupling to the continuum. The positions E_{res} (in units of mc^2) and decay widths Γ (in units of keV) of this state of the U-U system are listed in Table IV, for a range of internuclear distances. The quoted values were obtained by Padé extrapolation of CAP trajectories: $E_r = E(\eta = 0)$ as described above. The shift of the resonance position and broadening of the width are remarkable with the inclusion of the D-state ($\kappa = +2, -3$) channels, with smaller corrections to both the energy and the resonance width as a G-state ($\kappa = +4$) channel is coupled in with the hexadecapole potential.

TABLE IV. Position E_{res} and width Γ of the $1S\sigma$ supercritical resonance in the U_2^{183+} system at various internuclear separations. The cutoff order of the multipole expansion, as well as the set of channels included, is given at the top.

	$l_{\max} = 0$ ($\kappa = -1$)		$l_{\max} = 2$ ($\kappa = -1, +2, -3$)		$l_{\max} = 4$ ($\kappa = -1, +2, -3, +4$)			
R (fm)	E_{res} (m_ec^2)	Γ (keV)	E_{res} (m_ec^2)	Γ (keV)	E_{res} (m_ec^2)	Γ (keV)	$\tilde{E}_{\mathrm{res}}$ (m_ec^2)	$\tilde{\Gamma}$ (keV)
16	−1.58929	1.9849	−1.61287	2.2319	−1.61281	2.3131	−1.60494	2.1471
18	−1.48734	1.0755	−1.51525	1.2964	−1.51517	1.2957	−1.50877	1.2431
20	−1.39629	0.5050	−1.42778	0.6752	−1.42765	0.6744	−1.42240	0.6440
22	−1.31494	0.1927	−1.34926	0.3023	−1.34907	0.3016	−1.34471	0.2859
24	−1.24204	0.05332	−1.27853	0.1085	−1.27829	0.1080	−1.27462	0.1013
26	−1.17645	0.008486	−1.21454	0.02740	−1.21425	0.02719	−1.21115	0.02500
28	−1.11718	4.499×10^{-4}	−1.15641	3.7725×10^{-3}	−1.15607	3.7164×10^{-3}	−1.15342	3.3231×10^{-3}
30	−1.06340	1.156×10^{-6}	−1.10339	1.527×10^{-4}	−1.10301	1.4802×10^{-4}	−1.10073	1.2325×10^{-4}

TABLE V. Position E_{res} and width Γ of the $1S\sigma$ supercritical resonance in the (U-Cf)$^{189+}$ system at various internuclear separations. The cutoff order of the multipole expansion, as well as the set of channels included, is given at the top.

	$l_{\max} = 0$ ($\kappa = -1$)		$l_{\max} = 2$ ($\kappa = \pm 1, -2$)		$l_{\max} = 4$ ($\kappa = \pm 1, \pm 2, \pm 3, \pm 4$)			
R (fm)	E_{res} ($m_e c^2$)	Γ (keV)	E_{res} ($m_e c^2$)	Γ (keV)	E_{res} ($m_e c^2$)	Γ (keV)	$\tilde{E}_{\text{res}}$ ($m_e c^2$)	$\tilde{\Gamma}$ (keV)
16	−2.00635	8.1482	−2.00646	8.1501	−2.03730	8.7079	−2.03356	8.6391
20	−1.75793	4.0848	−1.75811	4.0874	−1.79918	4.687	−1.79674	4.6506
24	−1.56121	1.6967	−1.56145	1.6989	−1.60868	2.185	−1.60702	2.1669
28	−1.40354	0.5222	−1.40381	0.5235	−1.45422	0.819	−1.45304	0.8111
32	−1.27469	0.0931	−1.27498	0.0936	−1.32670	0.2130	−1.32583	0.2105
36	−1.16731	0.0051	−1.16761	0.0051	−1.21956	0.0277	−1.21890	0.0272
40	−1.07631	0.597×10^{-5}	−1.07661	$0.623 \cdot 10^{-5}$	−1.12813	70.0×10^{-5}	−1.12762	69×10^{-5}

The last two columns in Table IV list the resonance parameters recalculated using the effective U^{238} radius. The increased nuclear radius shifts the resonance positions to higher energies by only 0.2%–0.5% but narrows the widths more substantially, by 4%–16%.

The calculated resonance parameters for the U-Cf system are listed in Table V. The shift in the resonance position, as well as the increase in the resonance width, is again evident with the inclusion of more channels, especially at larger internuclear separations. Comparing the S-state ($\kappa = -1$, monopole approximation) results to those for the coupled S-P channels ($\kappa = \pm 1, -2$), one notices a small change. This is due to the weak dipole potential of the nearly charge-symmetric U-Cf system. There is a significant increase in Γ when the D-state ($\kappa = +2, -3$) channels are included, as well as smaller corrections as the F- and G-state ($\kappa = +3, \pm 4$) channels are coupled in with the higher-order multipoles. The combination of these effects is shown in the last two columns in Table V. The values for the first two cases (S- and S-P-channel couplings) are in agreement, to all digits shown, with the results in [6], which were obtained by expansion in a discrete Fourier sine-basis set.

As above, the resonance calclulations were repeated using the effective U^{238} and Cf^{251} radii, and the results ($\tilde{E}_{\text{res}}, \tilde{\Gamma}$) are shown in the last two columns in Table V. The corrections are much smaller than before: shifts of less than 0.2% in the resonance positions and narrowing of the widths by 0.8%–1.8%.

To verify that bound-state energies transition smoothly into the supercritical regime, the calculated resonance energies for the U-U and U-Cf systems were used to supplement the eigenenergies at subcritical internuclear separations. Points from both sides of the critical barrier were used for a polynomial fit, and the resulting interpolated critical distances agree with the values in Tables II and III to all digits shown. This was done for the most-converged calculations, i.e., those that include the largest number of channels and multipoles.

IV. CONCLUSIONS

We have extended the matrix representation-based analytic continuation method of Ref. [6] to make use of standard differential equation solvers in the finite domain $0 < r < r_a$. By choosing $r_a > 30$ natural units, we demonstrated an improvement in the quality of complex eigenenergy trajectories, which led to highly accurate stabilization values, as well as extrapolated resonance parameters.

We have shown that the supercritical regime in heavy-ion systems can be treated accurately by a multipole expansion of the two-center potential truncated at $l_{\max} = 4$, while the spinor wave functions can be truncated safely at $\kappa_{\min} = -3$ and $\kappa_{\max} = 4$. The truncations become less reliable at the critical distance, as shown by comparison with critical distance parameters for the U-U and U-Cf systems. The multipole expansion also has some convergence issues at the touching distance, where the $1S\sigma$ wave function is concentrated in the small-r region, such that multipoles higher than $l = 4$ can make a noticeable contribution. Thus, it will be of some interest to compare the present results with supercritical resonance calculations performed in two-center coordinates. The resonance parameters do show some dependence on the choice of nuclear charge radius; the change in the position is at or below the 1% level, while for the width it is of the order of a few percent, except for the U-U system, due to its relatively large effective nuclear radius.

ACKNOWLEDGMENTS

The authors would like to thank Johannes Schindler for assistance and discussion during the early stages of the work. This work was supported by NSERC Canada, and the German Academic Exchange Service (DAAD), and was carried out using the Shared Hierarchical Academic Research Computing Network (SHARCNET; www.sharcnet.ca). A.M. acknowledges the Ontario Graduate Scholarship Program for financial support.

[1] J. Reinhardt, B. Müller, and W. Greiner, Phys. Rev. A **24**, 103 (1981).

[2] J. Rafelski, L. Fulcher, and A. Klein, Phys. Rept. **38**, 227 (1978).

[3] W. Greiner, *Relativistic Quantum Mechanics: Wave Equations*, 3rd ed. (Springer, Berlin, 2000).
[4] J. C. Wells, V. E. Oberacker, A. S. Umar, C. Bottcher, M. R. Strayer, J.-S. Wu, and G. Plunien, Phys. Rev. A **45**, 6296 (1992).
[5] E. Ackad and M. Horbatsch, Phys. Rev. A **75**, 022508 (2007).
[6] E. Ackad and M. Horbatsch, Phys. Rev. A **76**, 022503 (2007).
[7] E. Ackad and M. Horbatsch, Phys. Rev. A **78**, 062711 (2008).
[8] C. Golabek and C. Simenel, Phys. Rev. Lett. **103**, 042701 (2009).
[9] E. Ackad and M. Horbatsch, J. Phys. A **38**, 3157 (2005).
[10] R. Lefebvre, M. Sindelka, and N. Moiseyev, Phys. Rev. A **72**, 052704 (2005).
[11] W. J. Thompson, *Angular Momentum: An Illustrated Guide to Rotational Symmetries for Physical Systems* (Wiley, New York, 1994).
[12] K. Rumrich, W. Greiner, G. Soff, K. Wietschorke, and P. Schlüter, J. Phys. B **22**, 165 (1989).
[13] B. Müller and W. Greiner, Z. Naturforsch. **31a**, 1-30 (1976).
[14] V. I. Lisin, M. S. Marinov, and V. S. Popov, Phys. Lett. B **91**, 20 (1980).
[15] I. I. Tupitsyn, Y. S. Kozhedub, V. M. Shabaev, G. B. Deyneka, S. Hagmann, C. Kozhuharov, G. Plunien, and Th. Stöhlker, Phys. Rev. A **82**, 042701 (2010).
[16] A. N. Artemyev, A. Surzhykov, P. Indelicato, G. Plunien and Th. Stöhlker, J. Phys. B **43**, 235207 (2010).
[17] V. M. Shabaev, J. Phys. B **26**, 1103 (1993).
[18] Y. S. Kozhedub, O. V. Andreev, V. M. Shabaev, I. I. Tupitsyn, C. Brandau, C. Kozhuharov, G. Plunien, and T. Stöhlker, Phys. Rev. A **77**, 032501 (2008).